Applied Catalysis B: Environmental 237 (2018) 1130–1138

Contents lists available at ScienceDirect

Applied Catalysis B: Environmental

journal homepage: www.elsevier.com/locate/apcatb

Covalently bonded 2D/2D O-g-C_3N_4/TiO_2 heterojunction for enhanced visible-light photocatalytic hydrogen evolution

Ruyi Zhong[a,b,1], Zisheng Zhang[a,1], Huqiang Yi[b], Lei Zeng[a], Chao Tang[a], Limin Huang[a,*], Meng Gu[b,*]

[a] Department of Chemistry, Southern University of Science and Technology, Shenzhen, 518055, China
[b] Department of Materials Science and Engineering, Southern University of Science and Technology, Shenzhen, 518055, China

ARTICLE INFO

Keywords:
2D/2D nanocomposite
Solvothermal synthesis
Covalent heterojunction
DFT calculations
Photocatalytic hydrogen evolution

ABSTRACT

Visible-light photocatalytic hydrogen evolution is a key step towards utilizing solar energy. Here we constructed covalently bonded oxidized graphitic C_3N_4/TiO_2 (O-g-C_3N_4/TiO_2) heterostructure with high surface area via an in-situ solvothermal synthetic strategy. The edge-anchoring of two-dimensional (2D) TiO_2 on 2D O-g-C_3N_4 was evidenced by the HAADF-STEM EDS mapping, EELS and XPS analysis. Density functional theory computations suggest strong affinity between TiO_2 and O-g-C_3N_4 2D structures through N—O—Ti covalent bonding, which drastically enhances the synergetic effect of the light absorption of O-g-C_3N_4 and high surface area of TiO_2. The as-formed heterojunction can remarkably boost the visible-light photocatalytic activity for H_2 evolution by 6.1 times compared to physical mixture of TiO_2 nanosheets (NS) and O-g-C_3N_4.

1. Introduction

Sun, the ultimate energy source of solar system, provides our mother planet with 120 000 TW annually through electromagnetic radiation [1]. Utilization of solar energy by photocatalysis is considered as one of the most promising strategies to meet the increasing energy and environmental demand of human society. In the 1970s, Fujishima and Honda split water into hydrogen and oxygen on sensitized TiO_2 photoanode under irradiation [2]. Since then, the solar-to-fuel conversion through semiconductor photocatalysis has been intensively studied [3–5].

Despite being the earliest milestone in photocatalysis, TiO_2 has never retired from the research frontier [6,7]. The band gap energy of TiO_2 (3.0 eV for rutile phase and 3.2 eV for anatase phase) provides sufficient overpotential to drive most of the desired redox reactions [4]. Stability in aqueous solution and biological nontoxicity made this low cost material commercially applicable on wide scales [8]. However, bulk TiO_2 materials often suffer from poor visible-range absorption (the majority in solar spectra) and rapid recombination of photo-induced electron-hole pairs. Although carrier migration can be facilitated by constructing TiO_2 nanostructures like nanosheets via quantum confinement effect [9], the absorption range remains in the ultraviolet region without elaborate chemical treatment. To tackle this problem, an effective method is to couple TiO_2 with a narrow band-gap material which provides visible-light absorption and improves separation efficiency of photo-induced charge carriers via formation of heterojunctions [10].

Among the extensively studied narrow band-gap photocatalysts, graphitic carbon nitride (g-C_3N_4) has been recently acknowledged as the next-generation photocatalyst by research community [11]. Besides outstanding visible-light response and earth-abundant nature, g-C_3N_4 is noted for its photostability and chemical tunability, which outperforms a wide range of metal-based narrow-band-gap materials such as Cu_2O, α-Fe_2O_3 and transition metal sulfides [12]. Constructing well-fabricated g-C_3N_4/TiO_2 nanocomposite with enhanced visible-light response is therefore becoming an emerging trend, and lots of synthetic attempts, such as co-calcination [13–21], hydrothermal treatment [22,23], and microwave-assisted synthesis [24], have proven to be successful. Up to now, mesoporous [17], core-shell [18,21], nanotube/nanosheet (1D/2D) [15], nanoparticle/nanosheet (0D/2D) [13,14,19,20,22–24] g-C_3N_4/TiO_2 heterojunctions have been reported. However, most investigations focused on tailoring the composition rather than modifying the interaction type that defines a heterojunction interface. In addition, these reported heterojunctions encounter an inevitable traffic congestion of charge carriers at interfaces [25,26]. The limitation could be surpassed by constructing a well-defined nanosheet/nanosheet (2D/2D) heterojunction [27,28]. Such 2D/2D heterojunction can provide large contact area to facilitate migration of charge carriers at contact

* Corresponding authors.
E-mail addresses: huanglm@sustc.edu.cn (L. Huang), gum@sustc.edu.cn (M. Gu).
[1] These authors contributed equally to this work.

https://doi.org/10.1016/j.apcatb.2017.12.066
Received 26 September 2017; Received in revised form 18 November 2017; Accepted 24 December 2017
Available online 11 January 2018
0926-3373/

interfaces and separation of electron-hole pairs, which is beneficial for photocatalytic application [29–31]. Moreover, a high-performance g-C_3N_4/TiO_2 photocatalyst for hydrogen evolution reaction (HER) under visible irradiation has not been reported yet.

In this work, we present a novel self-assembled 2D/2D O-g-C_3N_4/TiO_2 composite with enhanced visible-light photocatalytic activity for hydrogen evolution reaction (HER). The applied one-pot solvothermal synthesis is convenient, cost-effective and fluorine-free, while exhibiting high controllability of crystal phase and morphology. Two-dimensional nature of the individual component of the composite grants itself with large specific surface areas, pronounced quantum confinement effect and exposed active sites. The well-defined heterojunction between O-g-C_3N_4 and TiO_2 nanosheets is formed via covalent N—O—Ti linkage in-situ which is predicted by density functional theory (DFT) computation and confirmed with EELS and XPS. The strong orbital interactions invoke a band bending at interface, which facilitates migration of photo-induced charge carriers and extend the absorption range.

2. Experimental section

2.1. Materials

Poly(ethylene oxide)-block-poly(propylene oxide)-block-poly(ethylene oxide) triblock copolymer (Pluronic P123, $EO_{20}PO_{70}PEO_{20}$, M_W = 5800) was purchased from Sigma-Aldrich (USA). Titanium isopropoxide (TTIP), hydrochloric acid, ethylene glycol, melamine, ethanol, H_2PtCl_6 and triethanolamine (TEOA) was purchased from Aladdin Industrial Corporation (Shanghai, China). All reagents were used as-received without further purification.

2.2. Synthesis of raw TiO_2 nanosheets

The ultrathin TiO_2 nanosheets were prepared using an adopted solvothermal self-assembly method [32,33]. Namely, 1.05 g titanium isopropoxide (TTIP) was added into 0.74 g concentrated HCl under vigorous stirring for 15 min. Meanwhile, 200 mg P123 was dissolved in 3.8 mL ethanol by ultrasonication. The P123 ethanol solution was then added to the above TTIP solution, followed by continuous stirring for another 30 min. 5 mL of the precursor solution with 40 mL ethylene glycol was transferred to an 100 mL Telfon-lined autoclave and heated at 150 °C for 20 h. After cooling down naturally to room temperature, the precipitate was extensively washed with ethanol through centrifugation to remove organic templates and acids. After drying at 60 °C overnight, *ca.* 100 mg white solid was collected, which was denoted as TiO_2 nanosheets.

2.3. Synthesis of raw g-C_3N_4 nanosheets, O-g-C_3N_4 and H^+-g-C_3N_4

The raw g-C_3N_4 was prepared by thermal polymerization of melamine under air atmosphere [14]. In a typical procedure, 20 g of melamine powder was placed in a covered porcelain boat and heated in a muffle furnace at 550 °C for 2 h, at a heating rate of 5 °C/min. The resultant was grinded to yield a yellow powder. To mildly oxidize the g-C_3N_4 while maintaining the nanosheet morphology, two methods were adopted. The first one is a hydrothermal method [34]. 200 mg g-C_3N_4 was dispersed in 100 mL deionized water with assistance of 30 min ultrasonication. The suspension was then transferred into a 200 mL Teflon-lined autoclave and heated at 180 °C for 4 h. The resultant was centrifuged and dried overnight at 60 °C, which was denoted as O-g-C_3N_4. The second method is an adopted room-temperature acid treatment [35]. 500 mg raw g-C_3N_4 was added to 12.5 mL of concentrated HCl under vigorously stirring for 1 h. Reaction mixture was filtered, centrifuged and washed for several times to remove excessive HCl. The resultant yellow powder was denoted as H^+-g-C_3N_4.

2.4. Synthesis of O-g-C_3N_4/TiO_2, H^+-g-C_3N_4/TiO_2 and g-C_3N_4/TiO_2 composites

All composites were prepared by a bottom-up synthetic strategy of in-situ growth of TiO_2 NS on g-C_3N_4 substrates. Typically, 100 mg of pretreated or raw g-C_3N_4 was dispersed in 40 mL ethylene glycol by 30 min ultrasonication in a 100 mL Teflon-liner. 200 mg P123 was dispersed in 3.8 mL absolute ethanol by ultrasonication; 1.1 mL Titanium isopropoxide was added into 0.7 mL concentrated HCl and stirred for 15 min. Then P123 dispersion is added to this mixture, followed by 30 min stirring. 5 mL of mixed solution was transferred to the Teflon-liner with oxidized g-C_3N_4 suspension and heated at 150 °C for 20 h in an autoclave. The products were washed and centrifuged with deionized water and absolute ethanol for several times to remove organic templates and acids. Yellow precipitations were collected and dried at 60 °C overnight to obtain the final product. For O-g-C_3N_4/TiO_2, the ratios of TiO_2 and O-g-C_3N_4 were varied: 50, 100 and 200 mg O-g-C_3N_4 were added for samples of O-g-C_3N_4/TiO_2 1:2, 1:1 and 2:1, respectively. The catalyst was also prepared by physical mixing the as-synthesized TiO_2 NS and O-g-C_3N_4 (1:1 weight ratio with respect to TiO_2 NS) and denoted as O-g-C_3N_4 TiO_2 Mixed.

2.5. Characterization

Thermogravimetric (TGA) measurements were performed in a Mettler-Toledo TGA instrument. About 10 mg of each sample was placed in an alumina crucible and heated to 800 °C at a heating rate of 10 °C/min in an air flow. X-ray diffraction (XRD) patterns were acquired on a Rigaku Smartlab–9 kW X-ray diffractometer. Specific surface area and pore structure of each sample were determined by nitrogen sorption analysis using Micromeritics ASAP 2020. The electron microscopy data (EDS, HAADF STEM, EELS) were acquired using the aberration-corrected FEI Titan at 200 kV. The Titan microscope is equipped with an ultra-high brightness gun and super-X EDS detector. The EDS collection efficiency is about 50 times higher than a normal STEM. The EELS spectra were background-subtracted using routine power law method before the N K edge at 400 eV. The energy resolution of the EELS is around 1 eV based on the full width half maximum measurement of the zero loss peak. X-ray photoelectron spectroscopy (XPS) measurement was carried out with Thermo SCIENTIFIC ESCALAB 250Xi instrument using a monochromatized Al Kα as the excitation source. C 1 s signal at 284.8 eV was used to calibrate the binding energy (BE) and Shirley-type background was applied for each spectrum. UV–vis diffuse reflectance spectra of the samples were recorded using Lambda 950 UV/Vis/NIR spectrometer (Perkin Elmer) equipped with a diffuse reflenctance attachment with a spetralon-cotaed integrating sphere against $BaSO_4$ reference.

2.6. Photocatalytic testing

The photocatalytic HER experiments were performed using an online photocatalytic hydrogen generation system (CEL-SPH2N, AuLight, Beijing). A 300 W Xe lamp (CEL-HX300) equipped with a UV cutoff filter (UVIRCUT400, AuLight, Beijing, $\lambda > 400$ nm) was used as the visible light source, which was fan-cooled during the experiment. To maintain the ambient temperature of reaction system under irradiation, a liquid trap system with water circulation was used. In a typical test, 50 mg of photocatalyst was dispersed in 50 mL of aqueous solution containing 20 vol.% of TEOA, a cheap sacrificial reagent. 3 wt.% of Pt co-catalyst was photo-deposited uniformly on surface of photocatalyst using H_2PtCl_6 as precursor. Before irradiation, the suspension was degassed thoroughly by evacuation to remove dissolved gases. After an adequate photo-depositing period, the gaseous product was analyzed every hour. H_2 evolution was quantitatively determined by an online gas chromatography (GC-7890, thermal conductivity detector, molecular sieve 5Å, N_2 carrier, Yiyou, Shanghai).

2.7. Theoretical computation

DFT computations were performed using the Gaussian 09 program. B3LYP functional is adopted for all computations [36–39]. The LanL2DZ basis set, containing double-ξ valence with effective core potentials (ECPs) of Hay and Wadt, was used for Ti atoms. Polarization functions were also added to Ti (f = 1.566) for better precision. For all other atoms including H, C, N and O, 6–311 + G** basis set [40–42] was used. The geometric structures of all species were optimized in the gas phase. Harmonic vibrational frequencies were also computed, whose result showed that all reaction intermediates have no imaginary frequency. Solvation corrections were computed with the same functional and basis sets used in gas phase optimization, based on the gas-phased optimized geometries. SMD (Solvation Model Density) [43] was adopted, with ethylene glycol being the solvent, and temperature is set to be 150 °C. Solvation-corrected Gibbs energy values of all intermediates were calculated. A $Ti(OH)_4$ unit was used to represent TiO_2 oligomer to simplify the calculation. A trimer of basic g-C_3N_4 unit was constructed to represent the unoxidized part on O-g-C_3N_4 nanosheet. To evaluate the thermodynamic feasibility of bonding modes, the change in Gibbs free energy (ΔG) is calculated by ΔG = ΣG(products)-ΣG(reactants) for the reactions of bond formation. The reactions can be classified into two groups: coordination and condensation. The detailed interpretations for the two types of reactions are provided in Scheme S1.

3. Results and discussion

3.1. Physico-chemical properties

3.1.1. TGA

TGA measurements (Fig. S1) in flowing air were conducted to ascertain the composition and thermostability of the C_3N_4/TiO_2 composites. The compositions are listed in Table 1. The DTG peak at ca. 300 °C is ascribed to the decomposition of residual P123 on TiO_2 part, which is hard to remove by ethanol washing [44]. The resulted TiO_2 weight percentage in the composites is lower than the nominal content.

3.1.2. XRD

The crystalline phases of all precursor nanosheets and composites were determined by X-ray diffraction as shown in Fig. 1. It could be seen in Fig. 1a that g-C_3N_4, O-g-C_3N_4 and H^+-g-C_3N_4 all show (100) and (200) characteristic peaks without noticeable shift in diffraction angle, however, the intensities for the oxidized samples are slightly reduced. This result indicates that the crystal structure of g-C_3N_4 is predominantly preserved during hydrothermal treatment, while acid treatment leads to structural deterioration, consistent with the observation from TGA measurements. TiO_2 nanosheets show peaks with relatively low intensities, which is due to large amount of amorphous TiO_2 formed in the solvothermal process [44]. The peaks can be assigned to anatase (100), (200) and rutile (110), (220), respectively [33]. The peak intensities of anatase phase are much stronger than those of rutile phase, proving the phase selectivity of this fluorine-free synthetic method. This phase selectivity is maintained in all composite synthesis as shown in Fig. 1b. In addition, the characteristic peaks of TiO_2 and g-C_3N_4 were observed without shifts in peak location in these composite samples, which indicates that the in-situ growth did not significantly affect the crystallinity of both nanosheets, irrespective of the amount or type of g-C_3N_4.

3.1.3. N_2 sorption

N_2 sorption measurements were performed to investigate the textural characteristics of the obtained materials. Fig. S2 shows the N_2 sorption isotherms and the corresponding pore size distribution and Table 1 summarizes S_{BET}, V_{tot}, V_{meso} and average pore size. All isotherms are of type IV with H4 type hysteresis loops, indicating the co-existing of micropores and slit-shaped mesopores caused by the stacking of thin nanosheets, which can be observed from the wrinkles and irregular folding structures in the TEM images (Figs. S3 and S4). The S_{BET} of TiO_2 NS is 330 $m^2 g^{-1}$, close to the reported result [33]. The g-C_3N_4 family presents much smaller S_{BET} and lower porosity than TiO_2 NS, even though mild oxidation by hydrothermal treatment increases S_{BET} to 55 $m^2 g^{-1}$ and V_{tot} to 0.20 $cm^3 g^{-1}$. To be noted, the average pore size for the g-C_3N_4 family is much larger than TiO_2 NS, indicating the larger nanosheets size of the former. The composite samples all show higher S_{BET} and V_{tot} than their correspondent precursor g-C_3N_4. The increase in the porosity is ascribed to the TiO_2 component in the composite. O-g-C_3N_4/TiO_2 1:1 possesses S_{BET} of 263 $m^2 g^{-1}$, V_{tot} of 0.57 $cm^3 g^{-1}$, and average pore size of 14.7 nm. TiO_2 in O-g-C_3N_4/TiO_2 1:1 is likely to embody similar textural properties to that in TiO_2 NS. The even larger V_{tot} and average pore size of the composite than those of TiO_2 NS are ascribed to the presence of O-g-C_3N_4. Further increasing the amount of O-g-C_3N_4, however, reduces the porosity, since the porosity and surface area are mainly contributed by TiO_2 part. It is speculated that the introduction of O-g-C_3N_4 in the solvothermal synthesis does not exert significant influence on the templated growth and aggregation state of TiO_2 nanosheets. g-C_3N_4 may also not interfere much, due to few functional groups at its surface. Nevertheless, H^+-g-C_3N_4 probably results in some aggregation of TiO_2 NS due to protonation of amine groups caused by acid treatment, leading to the relatively less porosity.

Table 1
Physico-chemical properties of C_3N_4/TiO_2 composites and the precursors.

Entry	Catalyst	TiO_2[a] (wt.%)	S_{BET}[b] ($m^2 g^{-1}$)	V_{tot}[c] ($cm^3 g^{-1}$)	V_{meso}[d] ($cm^3 g^{-1}$)	Average pore size[e] (nm)
1	O-g-C_3N_4/TiO_2 1:1	37	263	0.57	0.53	8.7
2	O-g-C_3N_4/TiO_2 1:2	50	287	0.60	0.54	8.4
3	O-g-C_3N_4/TiO_2 2:1	21	171	0.43	0.40	10.1
4	g-C_3N_4/TiO_2 1:1	39	259	0.48	0.42	7.3
5	H^+-g-C_3N_4/TiO_2 1:1	33	163	0.17	0.13	4.3
6	O-g-C_3N_4 TiO_2 Mixed	35	n.d.	n.d.	n.d.	n.d.
7	TiO_2 NS	59	330	0.41	0.36	5.0
8	g-C_3N_4	0	12	0.12	0.12	43.5
9	O-g-C_3N_4	0	55	0.20	0.20	14.7
10	H^+-g-C_3N_4	0	19	0.12	0.12	25.8

[a] The TiO_2 content in the composite or TiO_2 NS is determined from TGA.
[b] Surface area (S_{BET}) is calculated by the Brunauer-Emmett-Teller (BET) method.
[c] Total pore volume (V_{tot}) was calculated from the saturation plateau at high relative pressures.
[d] Mesopore volume (V_{meso}) was calculated after subtraction of the micropore volume as obtained by the t-plot method.
[e] Average pore size was calculated from adsorption branches of the isotherms, based on the Barrett-Joyner-Halenda (BJH) model.

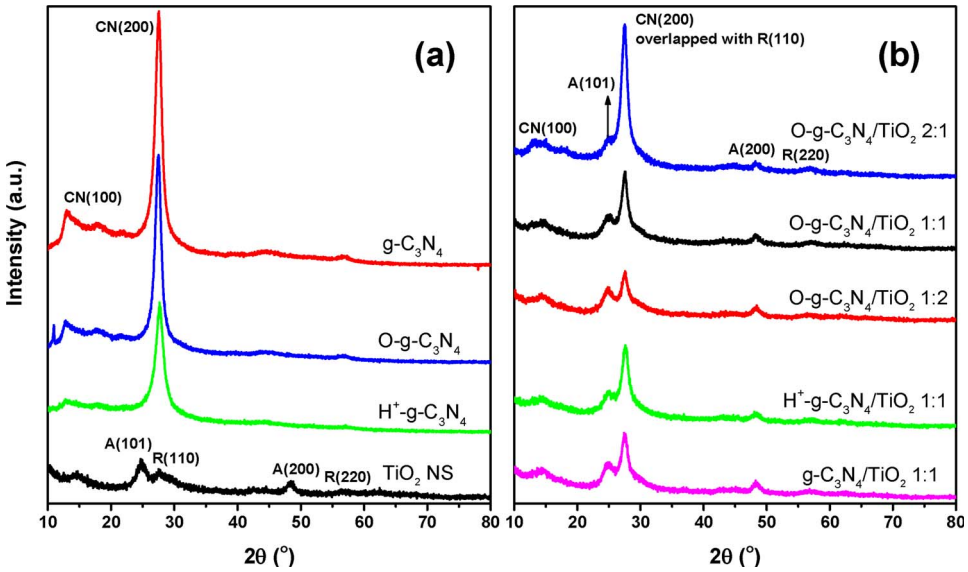

Fig. 1. XRD patterns of (a) TiO_2 NS, g-C_3N_4, O-g-C_3N_4, H^+-g-C_3N_4 and (b) composites of O-g-C_3N_4/TiO_2 with ratios of 1:1, 1:2, 2:1, g-C_3N_4/TiO_2 1:1 and H^+-g-C_3N_4/TiO_2 1:1.

3.2. Investigation on interfacial covalent bonding

3.2.1. Elemental distribution at interface

High-angle annular dark-field scanning TEM (HAADF-STEM) imaging of O-g-C_3N_4/TiO_2 1:1 shows fine interfacial structures. It can be seen in Fig. 2a that small ultrathin leaf-shaped nanosheets (around 50 nm) grow on the edge of much larger nanosheets. The elemental composition was revealed by energy-dispersive X-ray spectroscopy (EDS) mappings as shown in Fig. 2b–e. Overall morphology and elemental mapping can be found in Fig. S5. Elemental distribution indicates that the large nanosheet is O-g-C_3N_4 and the small nanoleaves at its edges are TiO_2. The individually grown ultrathin TiO_2 nanosheets, formed by template-assisted self-assembly, show extensive surface area which is evidenced by N_2 sorption results.

To investigate the interface between the two components, electron energy loss spectra (EELS) were obtained at different interface regions 1 and 2, and also at the pure TiO_2 leaf region, as is shown in Fig. 2f. N K edge, Ti L edge and O K edge can be observed at both interface regions 1 and 2. At the pure TiO_2 leaf region, only two-peak feature of the Ti L3 and L2 edge can be seen. No octahedral crystal field splitting feature is observed in the as-formed TiO_2, indicating a likely poor crystallinity of TiO_2 leaves. It corresponds well to the low-intensity XRD peaks as discussed earlier. The Ti and O signals increase and N K edge decreases in intensity gradually as it goes further away from the ("root") interface area. Both the Ti and N EELS edges are very pronounced at the interface, indicating the formation of the connected O-g-C_3N_4/TiO_2 heterojunction. In contrast, the N K edge disappears in the pure TiO_2 leaf region. The EELS results are in good agreement with the EDS mapping as shown in Fig. 2g. In addition, the O K edge for the TiO_2 leaf shows a clear two-peak feature in Fig. 2g. Peak 1 is narrower and sharper than peak 2 at the TiO_2 leaf. The O K edge peak 1 and 2 are wider at the interface region than the pure TiO_2 region. Based on the plural scattering theory, the peaks 1 and 2 are impacted heavily by the scattering of the fast electrons by the first and second nearest coordination shells

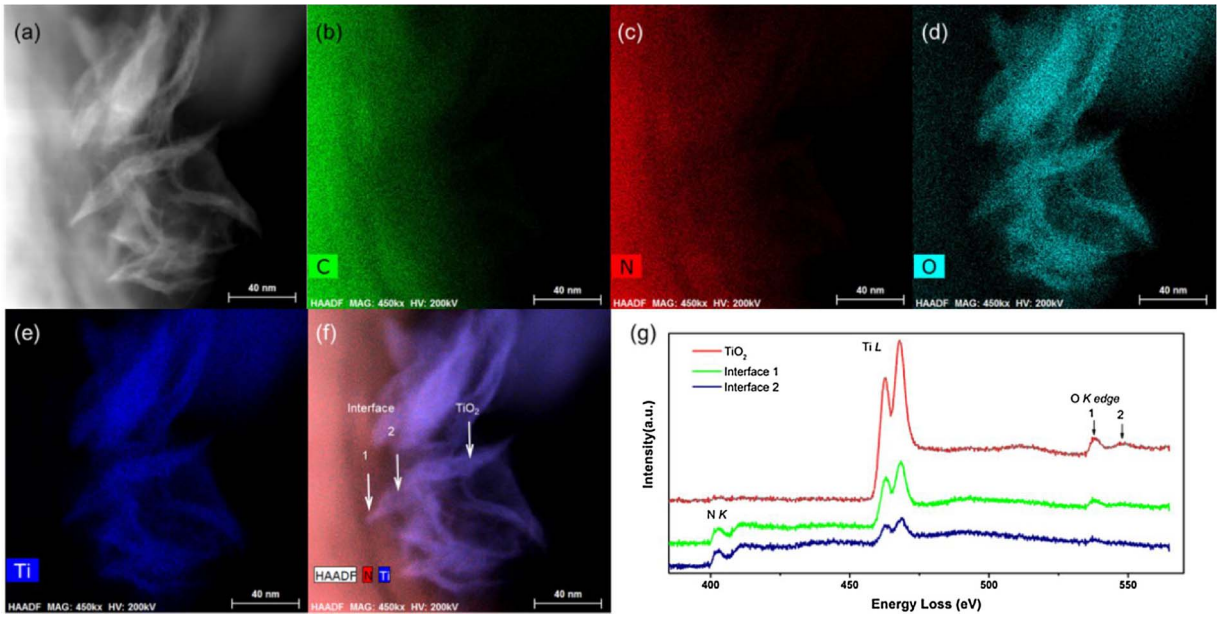

Fig. 2. (a) Representative HAADF-STEM image of O-g-C_3N_4/TiO_2 1:1 and (b) C, (c) N, (d) O, and (e) Ti EDS elemental maps of the corresponding area. (f) Superposed N, Ti and HAADF maps showing the interface regions and TiO_2 leaves. (g) EELS spectra from interface and TiO_2 region showing the N K edge, Ti L edge, and O K edge.

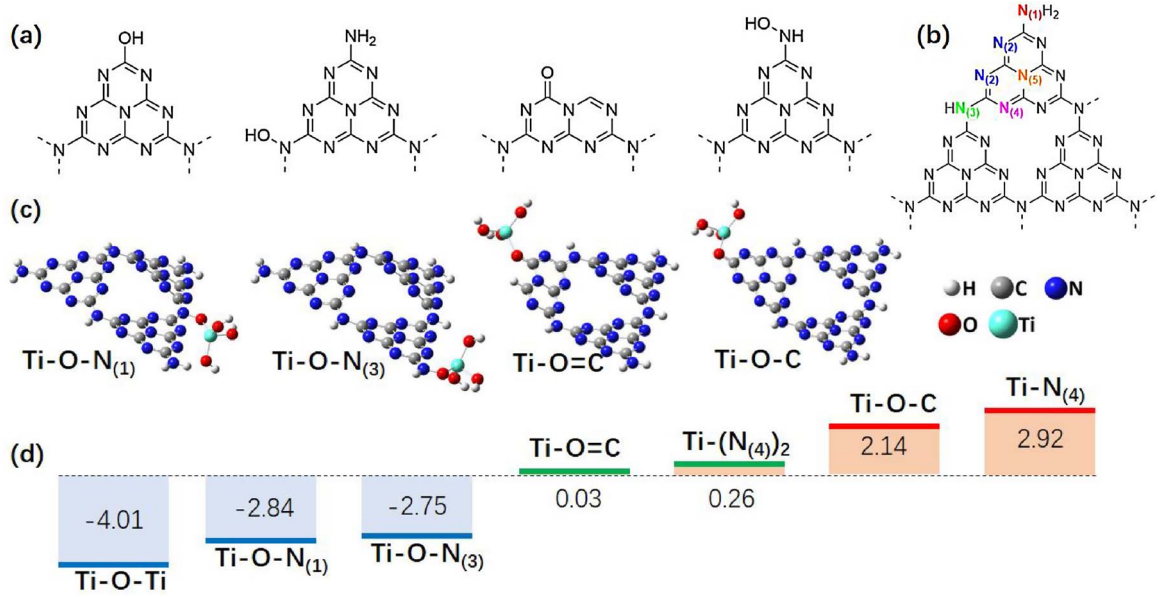

Fig. 3. (a) The functional groups introduced by mild oxidation, (b) different nitrogen sites on g-C_3N_4. (c) Bonding modes between O-g-C_3N_4 and TiO_2, and (d) ΔG of selected bonding modes (kcal/mol).

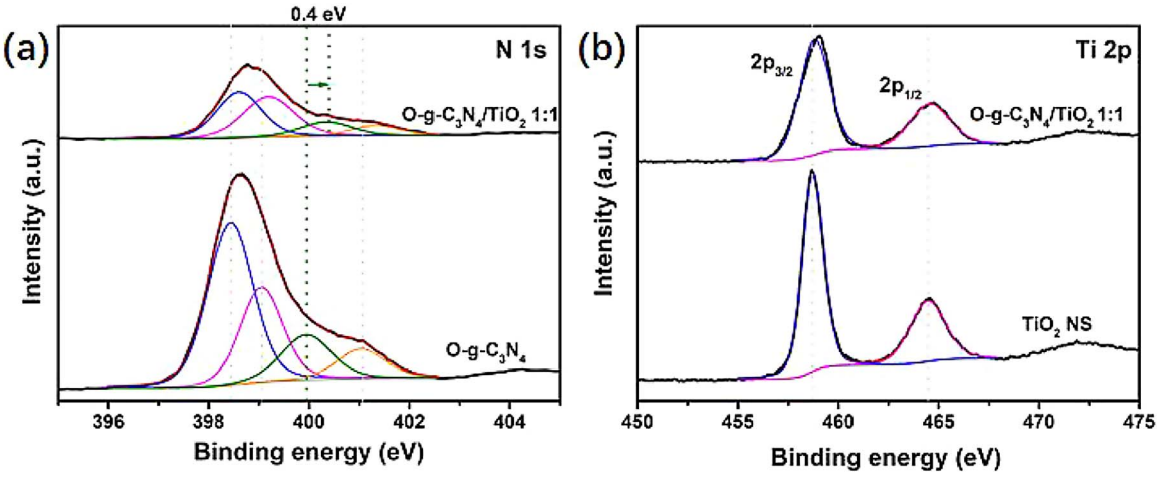

Fig. 4. XPS spectra of N 1s and Ti 2p in O-g-C_3N_4/TiO_2, O-g-C_3N_4 and TiO_2 NS.

around the O atoms, respectively [45]. The fact that the peaks of the O K edge get wider indicates the increased degree of disorder of the oxygen coordination environment at interfaces [45,46], probably resulting from the covalent bonding between TiO_2 NS and O-g-C_3N_4 formed during the solvothermal process.

3.2.2. DFT calculation

To investigate the bonding modes between O-g-C_3N_4 and TiO_2 nanosheets under solvothermal condition, thermodynamic calculations were conducted. A series of functional groups (Fig. 3a), which can be introduced to the edges of g-C_3N_4 by mild oxidation [34,35], were added to basic g-C_3N_4 unit to simulate oxidized O-g-C_3N_4 edges. Different nitrogen sites on O-g-C_3N_4 were treated respectively, as shown in Fig. 3b. P123 was neglected in this study to avoid otherwise huge computational cost. It is worth noting that the structural optimization leads to an energetically stable corrugated conformation of g-C_3N_4 rather than a planar one under solvothermal condition, as is shown in Fig. S6. The ridges form from corrugation, exposing active sites while keeping the band structure unchanged [47].

The Gibbs free energy change (ΔG) of formation of different bonding modes between $Ti(OH)_4$ unit and O-g-C_3N_4 and selected N-Ti, O-Ti distances are summarized in Table S1, and the corresponding optimized structures are shown in Fig. S7. All coordination bonding modes were calculated to be thermodynamically infeasible (ΔG > 0), including coordination of Ti with any C, O and N sites on O-g-C_3N_4 (Table S1, 1–13). Calculations also suggest that Ti—OH cannot condensate with C—OH or N—H on O-g-C_3N_4 (Table S1, 14–16). The only two thermodynamically feasible linkages between TiO_2 and O-g-C_3N_4 are the $N_{(1)}$—O—Ti and $N_{(3)}$—O—Ti that form through condensation between N—OH and Ti—OH. The formation is partially due to the stabilizing effect of neighboring N atoms. Therefore the calculations suggest a stronger affinity between TiO_2 oligomer and oxidized edges of O-g-C_3N_4 compared to its unoxidized regions. The four bonding modes enabled by the presence of oxygen-containing functional groups ($N_{(1)}$—OH, $N_{(3)}$—OH, C═O, C—OH) on O-g-C_3N_4 edges and seven bonding modes with the lowest ΔG are shown in Fig. 3c and d. The calculation results provide evidence for covalent bonding at composite interface through N—O—Ti bonding.

3.2.3. XPS

The bonding modes of O-g-C_3N_4, TiO_2 and O-g-C_3N_4/TiO_2 are analyzed by XPS as shown in Fig. 4. In the deconvoluted N 1s spectrum

of O-g-C_3N_4, four peaks at about 398.4, 399.0, 399.9 and 401.0 eV can be assigned to nitrogen in C—N, C═N, N—O and N—H bonds, respectively [34]. These four peaks can also be observed in the O-g-C_3N_4/TiO_2 composite, however, the peak corresponding to N—O shifted to higher binding energy (BE) by 0.4 eV, which should be caused by formation of N—O-Ti as predicted by DFT calculation. Electron-deficient Ti atom tends to lower the electron density of N—O system via Ti—O bond, weakening the shielding effect of N valence electrons, which increases the BE of N 1s electrons. The Ti 2p spectra of pure TiO_2 and composite both showed peaks of Ti $2p_{1/2}$ and Ti $2p_{3/2}$ at 458.7 and 464.4 eV, respectively [48]. There was no significant shift in BE of both peaks, which suggests the chemical state of Ti is not altered during solvothermal process regardless of the presence of O-g-C_3N_4. The well-fitted two peaks clearly exclude the presence of Ti—C [22], Ti—N [22] and Ti^{3+} [23] which, if exist, should have Ti $2p_{3/2}$ peaks located at 460.8, 462.1 and 463.3 eV, respectively. The XPS spectra of C 1s and O 1s (Fig. S8) cannot provide concrete evidence for N—O—Ti formation due to interference of adsorbed P123 surfactant.

3.2.4. Formation mechanism

Based on above experimental and theoretical results, a mechanism for the composite formation can be proposed as shown in Scheme 1. First, TTIP forms hydrated TiO_2 precursor oligomers during controlled hydrolysis. The oligomers are then confined inside the inverse lamellar micelles of P123 through hydrogen bonds in EG solution [33]. The tiny layered oligomer agglomerates are attached to edges of O-g-C_3N_4 via N—O—Ti covalent linkage. Thereafter, the attached oligomer agglomerates grows in-situ into leaf-shaped ultrathin TiO_2 nanosheets. After template removal, the O-g-C_3N_4/TiO_2 covalent heterojunction is successfully fabricated. The formation of N—O—Ti linkage at the interfaces could facilitate the separation and migration of photo-induced charge carriers through the heterojunction, which can improve the optical and photoelectrochemical properties.

3.3. Optical properties and photocatalytic activities

3.3.1. UV–vis DRS

UV-vis diffuse reflection spectra were collected and analyzed to investigate optical absorption and band structure of all samples (Fig. 5). As shown in Fig. 5a, TiO_2 nanosheets have outstanding UV absorption but zero absorption above 400 nm. In contrast, the raw g-C_3N_4 has a superior visible-range absorption. Both oxidation methods, namely hydrothermal and acid treatments, only introduced minor defects and functional groups which do not alter absorption range dramatically. Fig. 5b displays the UV–vis absorption spectra of all composites. The g-C_3N_4/TiO_2 1:1 composite exhibits no apparent widening in absorption range, which can be explained by absence of effective linkages between TiO_2 and g-C_3N_4 nanosheets as suggested by DFT calculation. On the contrary, O-g-C_3N_4/TiO_2 and H^+-g-C_3N_4/TiO_2 composites show broader absorption range due to formation of covalent heterojunctions via N—O—Ti bonds. Among all composites the O-g-C_3N_4/TiO_2 1:1 sample experiences the most pronounced broadening in absorption range.

The corresponding band gap energy can be derived according the Kubella-Munk function [49], as is shown in Fig. 5c and d. The g-C_3N_4 family was treated as direct gap semiconductor while all other samples were treated as indirect ones. The g-C_3N_4 family has narrower band gap than TiO_2 nanosheets. Mild oxidation resulted in a slight change in band gap energy of g-C_3N_4. However, all of the composites showed significantly narrower band gap than any of the pure nanosheets. The decrease in band gap energy is likely caused by the formation of heterojunction between two materials with staggered band structures. O-g-C_3N_4/TiO_2 has the narrowest band gap among the three composite types, suggesting a stronger interaction at its heterojunction interfaces than those of g-C_3N_4/TiO_2 and H^+-g-C_3N_4/TiO_2. By reducing the ratio of TiO_2 and O-g-C_3N_4 in the composite, the contribution of such effect can be strengthened, leading to a narrower band gap and therefore extending the spectral response. Band gap tuning in similar composite systems can be achieved by functionalizing the precursors as well as adjusting the composition.

3.3.2. Photocatalytic hydrogen evolution

The photocatalytic activity of the as-prepared samples was evaluated by hydrogen evolution from water under visible-light irradiation (wavelength > 400 nm). TiO_2 exhibits no photocatalytic activity since its bandgap energy is too high for visible-light to induce electron excitation. g-C_3N_4 showed a low hydrogen evolution of 180.5 μmol g^{-1} h^{-1}, suffering from fast recombination of photo-induced electron-pairs and small surface area. The problem is not settled even after mild oxidation, with O-g-C_3N_4 and H^+-C_3N_4 exhibiting just slightly improved photocatalytic activity. In contrast, all composite samples display a significant boost in hydrogen evolution. The O-g-C_3N_4/TiO_2 1:1 composite shows the best performance in hydrogen evolution, reaching 587.1 μmol g^{-1} h^{-1} which is 6.1 times the physical mixture, and 3.2 times the pure O-g-C_3N_4. This boost in photocatalytic activity can be attributed to the formation of covalent bonding at heterojunction interfaces. Through N—O—Ti linkage which is predicted by DFT computation and confirmed by XPS and EELS, the photo-induced electrons from O-g-C_3N_4 can migrate to TiO_2 with high efficiency and the recombination of photo-induced electron-hole pairs is suppressed. The efficient heterojunction may also lead to band bending at the interface region, which lowers the local band gap energy and broadens

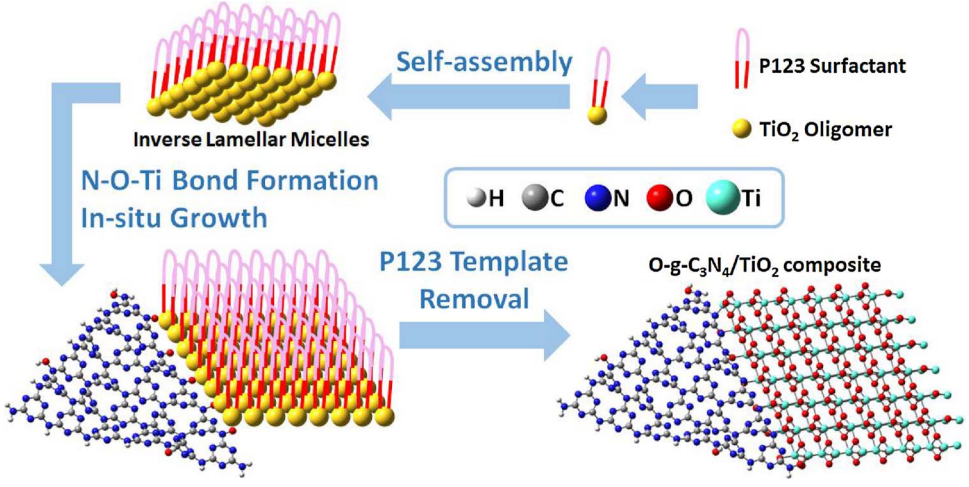

Scheme 1. Schematic of the synthesis of O-g-C_3N_4/TiO_2 composite.

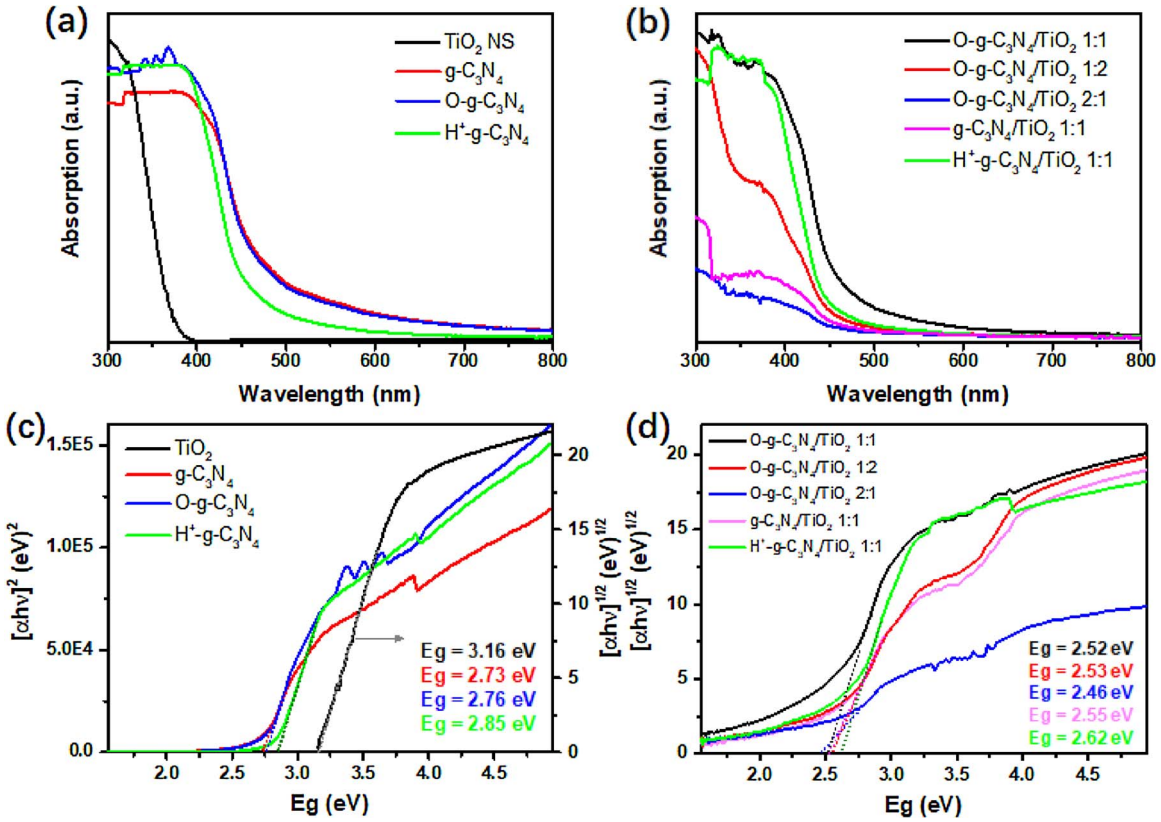

Fig. 5. UV–vis DRS of (a) TiO_2 NS, g-C_3N_4, O-g-C_3N_4, H^+-g-C_3N_4 and (b) composites of O-g-C_3N_4/TiO_2 with ratios of 1:1, 1:2, 2:1, g-C_3N_4/TiO_2 1:1 and H^+-g-C_3N_4/TiO_2 1:1. (c, d) Corresponding plots of $(\alpha h\nu)^2$ or $(\alpha h\nu)^{1/2}$ versus photon energy ($h\nu$) for the band gap energies of samples in (a, b).

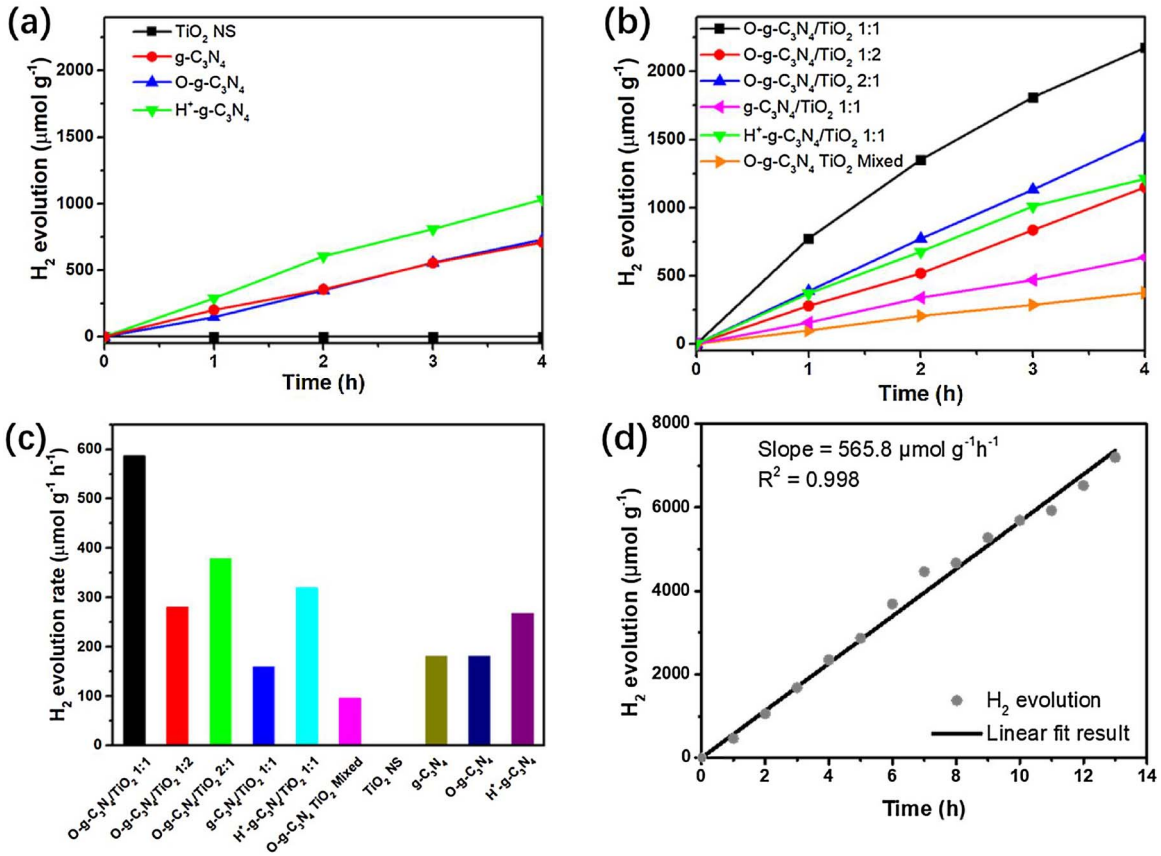

Fig. 6. Hydrogen evolution plot versus time of (a) TiO_2 NS, g-C_3N_4, O-g-C_3N_4, H^+-g-C_3N_4 and (b) composites of O-g-C_3N_4/TiO_2 with ratios of 1:1, 1:2, 2:1, g-C_3N_4/TiO_2 1:1, H^+-g-C_3N_4/TiO_2 1:1 and O-g-C_3N_4 TiO_2 Mixed. (c) Hydrogen evolution rates of all tested photocatalysts. (d) Stability test of O-g-C_3N_4/TiO_2 1:1 sample under the same reaction conditions.

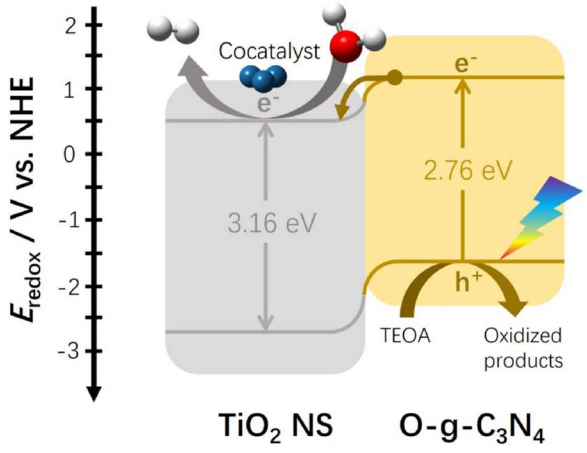

Scheme 2. Proposed mechanism for photocatalytic hydrogen evolution on O-g-C_3N_4/TiO_2 1:1 composite under visible-light irradiation.

the absorption range [50,51]. In addition, the 2D nanostructure provides large specific surface area for cocatalyst loading, reactant adsorption and mass transfer acceleration. To optimize the benefits from all discussed effects, composites made with various weight ratios of O-g-C_3N_4 and TiO_2 were tested. The 1:1 ratio was found to maximize the construction of N—O—Ti heterojunction without compromising the merit of specific surface area. Fig. 6d shows the stability test result for O-g-C_3N_4/TiO_2 1:1 sample under the same reaction conditions. The hydrogen evolution rate stays at about 565.8 μmol g^{-1} h^{-1} during the 13-h irradiation, indicating that the as-fabricated N—O—Ti covalent heterojunction successfully achieves remarkably high photocatalytic activity as well as stability. With facile preparation and remarkably enhanced photocatalytic activity, the as-prepared O-g-C_3N_4/TiO_2 might provide insights for design and synthesis of high-performance O-g-C_3N_4/metal oxide photocatalysts with covalent heterojunctions.

The mechanism for photocatalytic HER on O-g-C_3N_4/TiO_2 composite under visible-light irradiation is illustrated in Scheme 2. Incident photons with sufficient energy excite electrons in valence band of O-g-C_3N_4 to its conduction band. The photo-induced holes in valence band of O-g-C_3N_4 are captured by TEOA, while the photo-induced electrons migrate through covalent N—O—Ti heterojunction into the valence band of TiO_2 nanosheets. The photo-induced electrons finally reach uniformly deposited Pt cocatalyst at vast TiO_2 surface where the electrons reduce water to hydrogen gas. Heterojunction defined by N—O—Ti linkages results in efficient charge carrier separation at interfaces and band bending effect which further widens the absorption range, enhancing the photocatalytic activity of the composite.

4. Conclusions

Covalently bonded O-g-C_3N_4/TiO_2 heterojunctions were successfully fabricated via a facile one-pot solvothermal synthetic method. In this strategy, using O-g-C_3N_4 as the substrate and P123 as the soft templating agent, ultrathin and uniform TiO_2 nanoleaves grew in-situ onto O-g-C_3N_4 edges. The N—O—Ti covalent bonding at heterojunction interfaces is evidenced by experimental characterization and DFT computation. Compared to composites derived from other types of g-C_3N_4 precursors (raw g-C_3N_4 and H^+-g-C_3N_4) and physical mixture, O-g-C_3N_4/TiO_2 exhibited superior visible-light activity and high stability for photocatalytic hydrogen evolution reaction, due to the facilitated charge carrier migration through the heterojunction defined by covalent interfacial N—O—Ti bonding.

Acknowledgements

This work was financially supported by Southern University of Science and Technology (SUSTech) start fund through Shenzhen Peacock Talent program, the basic research fund of Shenzhen (JCYJ20150507170334573), the technical research fund of Shenzhen (JSGG20160427105120572), and Guangdong Innovative and Entrepreneurial Research Team Program (No. 2016ZT06N532). This work was also supported by the Pico Center and High Performance Computing Center at SUSTech that receives support from Presidential fund and Development and Reform Commission of Shenzhen Municipality.

Appendix A. Supplementary data

Supplementary data associated with this article can be found, in the online version, at https://doi.org/10.1016/j.apcatb.2017.12.066.

References

[1] P.D. Tran, L.H. Wong, J. Barber, J.S.C. Loo, Energy Environ. Sci. 5 (2012) 5902–5918.
[2] A. Fujishima, K. Honda, Nature 238 (1972) 37–38.
[3] C. Acar, I. Dincer, G.F. Naterer, Int. J. Energy Res. 40 (2016) 1449–1473.
[4] S.N. Habisreutinger, L. Schmidt-Mende, J.K. Stolarczyk, Angew. Chem. Int. Ed. 52 (2013) 7372–7408.
[5] C. Liu, N.P. Dasgupta, P. Yang, Chem. Mater. 26 (2013) 415–422.
[6] R. Fagan, D.E. McCormack, D.D. Dionysiou, S.C. Pillai, Mater. Sci. Semicon. Proc. 42 (Part 1) (2016) 2–14.
[7] J. Schneider, M. Matsuoka, M. Takeuchi, J. Zhang, Y. Horiuchi, M. Anpo, D.W. Bahnemann, Chem. Rev. 114 (2014) 9919–9986.
[8] A. Mills, S. Lee, J. Photochem. Photobiol. A 152 (2002) 233–247.
[9] P.C.P. Andrade, Int. J. Quantum Chem. 112 (2012) 3325–3332.
[10] Y. Wang, Q. Wang, X. Zhan, F. Wang, M. Safdar, J. He, Nanoscale 5 (2013) 8326–8339.
[11] W. Ong, L. Tan, Y.H. Ng, S. Yong, S. Chai, Chem. Rev. 116 (2016) 7159–7329.
[12] L. Zhou, H. Zhang, H. Sun, S. Liu, M.O. Tade, S. Wang, W. Jin, Catal. Sci. Technol. 6 (2016) 7002–7023.
[13] K. Li, S. Gao, Q. Wang, H. Xu, Z. Wang, B. Huang, Y. Dai, J. Lu, ACS Appl. Mater. Interfaces 7 (2015) 9023–9030.
[14] J. Li, M. Zhang, Q. Li, J. Yang, Appl. Surf. Sci. 391 (Part B) (2017) 184–193.
[15] J. Li, M. Zhang, X. Li, Q. Li, J. Yang, Appl. Catal. B 212 (2017) 106–114.
[16] M. Reli, P. Huo, M. Šihor, N. Ambrožová, I. Troppová, L. Matějová, J. Lang, L. Svoboda, P. Kuśtrowski, M. Ritz, P. Praus, K. Kočí, J. Phys. Chem. A 120 (2016) 8564–8573.
[17] R. Hao, G. Wang, H. Tang, L. Sun, C. Xu, D. Han, Appl. Catal. B 187 (2016) 47–58.
[18] Y. Wang, W. Yang, X. Chen, J. Wang, Y. Zhu, Appl. Catal. B 220 (2018) 337–347.
[19] S. Zhou, Y. Liu, J. Li, Y. Wang, G. Jiang, Z. Zhao, D. Wang, A. Duan, J. Liu, Y. Wei, Appl. Catal. B 158 (2014) 20–29.
[20] N. Boonprakob, N. Wetchakun, S. Phanichphant, D. Waxler, P. Sherrell, A. Nattestad, J. Chen, B. Inceesungvorn, J. Colloid Interface Sci. 417 (2014) 402–409.
[21] W. Wang, J. Fang, S. Shao, M. Lai, C. Lu, Appl. Catal. B 217 (2017) 57–64.
[22] Z. Lu, L. Zeng, W. Song, Z. Qin, D. Zeng, C. Xie, Appl. Catal. B 202 (2017) 489–499.
[23] K. Li, Z. Huang, X. Zeng, B. Huang, S. Gao, J. Lu, ACS Appl. Mater. Interfaces 9 (2017) 11577–11586.
[24] X. Wang, W. Yang, F. Li, Y. Xue, R. Liu, Y. Hao, Ind. Eng. Chem. Res. 52 (2013) 17140–17150.
[25] B. Lin, H. Li, H. An, W. Hao, J. Wei, Y. Dai, C. Ma, G. Yang, Appl. Catal. B 220 (2018) 542–552.
[26] Z. Zhang, J. Huang, M. Zhang, Q. Yuan, B. Dong, Appl. Catal. B 163 (2015) 298–305.
[27] Q. Wang, W. Wang, L. Zhong, D. Liu, X. Cao, F. Cui, Appl. Catal. B 220 (2018) 290–302.
[28] C. Tan, X. Cao, X. Wu, Q. He, J. Yang, X. Zhang, J. Chen, W. Zhao, S. Han, G. Nam, M. Sindoro, H. Zhang, Chem. Rev. 117 (2017) 6225–6331.
[29] J. Wang, L. Tang, G. Zeng, Y. Deng, Y. Liu, L. Wang, Y. Zhou, Z. Guo, J. Wang, C. Zhang, Appl. Catal. B 209 (2017) 285–294.
[30] W. Ong, L. Tan, S. Chai, S. Yong, A.R. Mohamed, Nano Energy 13 (2015) 757–770.
[31] L. Yuan, M. Yang, Y. Xu, Nanoscale 6 (2014) 6335–6345.
[32] B. Yan, P. Zhou, Q. Xu, X. Zhou, D. Xu, J. Zhu, RSC Adv. 6 (2016) 6133–6137.
[33] Z. Sun, T. Liao, Y. Dou, S.M. Hwang, M. Park, L. Jiang, J.H. Kim, S.X. Dou, Nat. Commun. 5 (2014) 3813–3821.
[34] L. Ming, H. Yue, L. Xu, F. Chen, J. Mater. Chem. A 2 (2014) 19145–19149.
[35] C. Dong, Z. Ma, R. Qie, X. Guo, C. Li, R. Wang, Y. Shi, B. Dai, X. Jia, Appl. Catal. B 217 (2017) 629–636.
[36] S.H. Vosko, L. Wilk, M. Nusair, Can. J. Phys. 58 (1980) 1200–1211.
[37] W. Yang, R.G. Parr, C. Lee, Phys. Rev. B 37 (1988) 785–789.
[38] A.D. Becke, J. Chem. Phys. 98 (1993) 5648–5652.
[39] P.J. Stephens, F.J. Devlin, C.F. Chabalowski, M.J. Frisch, J. Phys. Chem. 98 (1994) 11623–11627.
[40] P.C. Hariharan, J.A. Pople, Theor. Chim. Acta 28 (1973) 213–222.
[41] M.S. Gordon, Chem. Phys. Lett. 76 (1980) 163–168.

[42] R.C. Binning, L.A. Curtiss, J. Comput. Chem. 11 (1990) 1206–1216.
[43] A.V. Marenich, C.J. Cramer, D.G. Truhlar, J. Phys. Chem. B 113 (2009) 6378–6396.
[44] J. Yang, Y. Jiang, L. Li, E. Muhire, M. Gao, Nanoscale 8 (2016) 8170–8177.
[45] D.J. Wallis, N.D. Browning, J. Am. Ceram. Soc. 80 (1997) 781–785.
[46] J.P. Buban, M. Chi, D.J. Masiel, J.P. Bradley, B. Jiang, H. Stahlberg, N.D. Browning, J. Mater. Res. 24 (2009) 2191–2199.
[47] L.M. Azofra, D.R. MacFarlane, C. Sun, Phys. Chem. Chem. Phys. 18 (2016) 18507–18514.
[48] Y. Xin, Y. Lu, C. Han, L. Ge, P. Qiu, Y. Li, S. Fang, Mater. Res. Bull. 87 (2017) 123–129.
[49] W. Zhao, W. Ma, C. Chen, J. Zhao, Z. Shuai, J. Am. Chem. Soc. 126 (2004) 4782–4783.
[50] P. Suyana, P. Ganguly, B.N. Nair, A.P. Mohamed, K.G.K. Warrier, U.S. Hareesh, Environ. Sci. Nano 4 (2017) 212–221.
[51] C. Zhang, Y. Chen, J. Huang, X. Wu, L. Li, W. Yao, J. Tersoff, C. Shih, Nat. Commun. 7 (2016) 10349–10354.